

PAPER

# Experimental constraint on the radial mode number of the geodesic acoustic mode from multi-point Langmuir probe measurements in MAST Ohmic plasma

To cite this article: B Hnat *et al* 2018 *Plasma Phys. Control. Fusion* **60** 085016

View the [article online](#) for updates and enhancements.

## Related content

- [Electromagnetic characteristics of geodesic acoustic mode in the COMPASS tokamak](#)  
J. Seidl, J. Krbec, M. Hron *et al*.
- [Review Article](#)  
Akihide Fujisawa
- [GAM observation in the TUMAN-3M tokamak](#)  
V V Bulanin, L G Askinazi, A A Belokurov *et al*.

## Recent citations

- [Overview of new MAST physics in anticipation of first results from MAST Upgrade](#)  
J.R. Harrison *et al*



**IOP | ebooks™**

Bringing you innovative digital publishing with leading voices to create your essential collection of books in STEM research.

Start exploring the collection - download the first chapter of every title for free.

# Experimental constraint on the radial mode number of the geodesic acoustic mode from multi-point Langmuir probe measurements in MAST Ohmic plasma

B Hnat<sup>1</sup> , S Gadgil<sup>1</sup>, A Kirk<sup>2</sup>, F Militello<sup>2</sup> , N Walkden<sup>2</sup>  and the MAST Team

<sup>1</sup>Physics Department, University of Warwick, Coventry, CV4 7AL, United Kingdom

<sup>2</sup>EURATOM/CCFE Fusion Association, Culham Science Centre, Abingdon, OX14 3DB, United Kingdom

E-mail: [b.hnat@warwick.ac.uk](mailto:b.hnat@warwick.ac.uk)

Received 12 January 2018, revised 7 June 2018

Accepted for publication 19 June 2018

Published 2 July 2018



CrossMark

## Abstract

Reciprocating Mach probe data is used to estimate the radial wave number of oscillatory zonal flows in Ohmic MAST plasma. An intermittent  $\sim 10$  kHz mode, previously identified as a geodesic acoustic mode (GAM), is detected in the wavelet decomposition and windowed spectra of plasma potential fluctuations of the MAST tokamak edge plasma. Two-points phase differencing technique is then applied to probe pins with radial and poloidal separations giving an estimate of the radial wave number at the desired range of frequencies. The phase velocity of propagation and an estimate of the shearing rate of the GAM is obtained. We measure the radial mode number range  $k_r \approx 0.3\text{--}1.0\text{ cm}^{-1}$  and a radial propagation speed of up to  $\sim 1\text{ km s}^{-1}$ . The GAM shearing rate is an order of magnitude smaller than the growth rate of drift-like turbulence. These results are consistent with the estimates obtained previously from multi-fluid numerical simulations of GAM in MAST.

Keywords: spherical tokamak, geodesic acoustic mode, radial mode structure

(Some figures may appear in colour only in the online journal)

## 1. Introduction

The anisotropic properties of drift wave turbulence (DWT) lead to the development of sheared flows, known as zonal flow (ZF) [1], which are considered distinct from the residual poloidal flows, called zero frequency zonal flows (ZFZF) [2]. These flows can regulate the global confinement properties of magnetically confined plasma by suppressing turbulent transport across the magnetic field [3, 4]. It is believed that large scale flows are essential in the transition to high-confinement mode (H-mode), with the edge plasma turbulence being substantially reduced during the transition [5–7]. In a slab geometry, ZF are stationary and have zero frequency, that is, their radial group velocity is zero [8]. In toroidal geometry, the curvature and the inhomogeneous magnetic field induce coupling of  $m = 0$  electrostatic potential to the

higher  $m$ -number density fluctuations with a finite frequency. This finite frequency compressible oscillation is called geodesic acoustic mode (GAM). The local dispersion relation for the GAM has been derived from various plasma models and the leading term is  $\omega_{G,l} \sim c_s/R_0$ , where  $c_s$  is the local sound speed and  $R_0$  is the major radius [9–12].

Compressible GAM fluctuations are heavily Landau damped for small safety factors  $q(r) \equiv rB_t/R_0B_p$ , where  $B_t$  and  $B_p$  are toroidal and poloidal magnetic field components, respectively. In the usual tokamak configuration and in the low-confinement mode (L-mode)  $q(r)$  increases toward the edge of the plasma and thus GAM is confined to the edge region in L-mode plasmas. There is substantial evidence that the GAM is a global mode, with a complex radial mode structure that does not simply follow the linear local dispersion relation. Indeed, observations [13–17] and numerical

simulations [18, 19] found a series of plateaus with nearly constant frequency spanning large fractions of minor radius. The aim of this work is to estimate the characteristic size of this radial structure based on Langmuir Mach probe measurements at the edge region of the Ohmic MAST plasmas.

The radial propagation of oscillatory ZF and the presence of compressible GAM fluctuations add new physics to the ZFZF-GAM-DWT interactions. GAM pressure fluctuations are nonlinearly advected by ZFZF and can transfer the energy to small scales providing a natural saturation mechanism for the ZF amplitudes [20]. In terms of linear effects, GAM introduces new spatial and temporal scales into the system. The GAM radial mode number  $k_r$  gives a shearing rate of turbulent eddies  $\gamma_{\text{sh}} \approx k_r V_G$ , where  $V_G$  is the poloidal ZF amplitude. The importance of the shearing mechanism depends on a time scale  $\tau_{k_r, p_r}$ , which reflects temporal coherence of turbulence wave packets with mode number  $p_r$  and the GAM [21]. The appearance of the GAM group velocity, due to its finite frequency, also permits some resonant-like interactions between GAMs and the turbulence. For example, taking  $\tau_{k_r, p_r} \sim |(v_{\text{gr}}^G - v_{\text{ph}}^G)k_r|^{-1}$  we obtain an infinite correlation time of turbulent structure propagating with the group velocity  $v_{\text{gr}}^T = v_{\text{ph}}^G$ .

The radial wave number of the GAM can be constrained by a few relatively simple arguments. The amplitude of the normalised GAM density  $n_1 = n/n_0$  and the electrostatic potential  $\phi_1 = e\phi/T_e$  fluctuations are related,  $n_1 \approx k_r \rho_p \phi_1 \sin \theta$ , where  $\rho_p$  is the proton gyroradius, and  $\theta$  is a poloidal angle. For JET plasma, where both,  $n_1$  and  $\phi_1$  can be measured simultaneously, this relation gives an estimate of  $0.6 \leq k_r \rho_p \leq 0.9$  for  $\theta = 75^\circ - 80^\circ$  [14]. Such estimation cannot be made on MAST because the measurements are collected at  $\theta \approx 0^\circ$ , making GAM density fluctuations very small and difficult to extract. The simplest analytical constrain of the GAM radial wavenumber can be obtained considering the finite gyroradius effects, which lead to the expression  $(1 - k_r^2 \rho_p^2) \omega_G^2 = \omega_{G,l}^2$  [22]. Since the observed frequency  $\omega_G$  is a complicated function the geometrical factors and the background Mach number, this expression provides only an upper limit  $k_r \rho_p \leq 1$ . Numerical studies have found the most unstable mode for drift/ITG turbulence at  $k_\theta \rho_p \approx 0.3$ . Nonlinear interactions of turbulent structures transfer the energy to larger spatial scales, thus, assuming wave number isotropy  $k_\theta \approx k_r$ , GAM's radial wave number should obey  $k_r \rho_p < 0.3$ . Global multi-fluid simulations have also been used to model GAMs directly, for the realistic MAST like Ohmic discharges. These simulations found a relatively narrow range of wave numbers  $k_r \rho_p \approx 0.05 - 0.15$  [19].

Here, we use MAST reciprocating Mach probe data to estimate the value of  $k_r$  directly, using the instantaneous phase difference technique applied to radially and poloidally separated probe pins measuring the electrostatic floating potential. We employ a modified Beall algorithm [23], which allows us to obtain statistically significant estimates of the wave number for short time intervals when the reciprocating probe position is relatively constant. A similar multi-point method has been

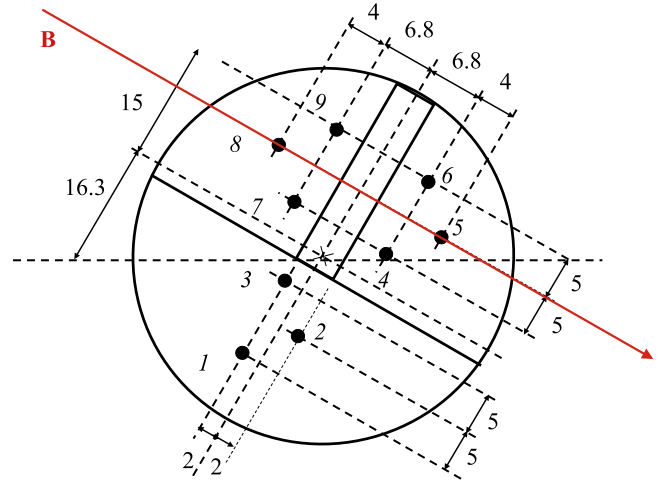


**Figure 1.** (a) Langmuir Mach probe with separations of different pins in millimetres. Pins 1, 2 and 3 are radially offset by 8 mm from all other pins.

applied before in ZF/GAM studies [24, 25], neglecting the poloidal wave number contribution. This is justified when a large scale separation exists between turbulent and GAM dynamical scales and the GAM energy significantly exceeds turbulent energy. Here, we will show that for the MAST edge plasma, and on the scales of the Mach probe pins separation, the estimate of GAM radial wave number is affected by the large poloidal wave numbers, but can be recovered by averaging the joint wave number-frequency spectrum over all poloidal wave numbers. We believe that this work presents the first estimate of the radial wave number of the GAM in a spherical tokamak. Our results are consistent with previous numerical [19] and experimental [24] studies and give  $0.05 < k_r \rho_p < 0.15$ . We find more power at larger wave numbers when the probe is approximately 2.5 cm from the LCFS and a small wave number of  $k_r \rho_p \sim 0.05$  when the probe is near its maximum displacement of 4.5 cm inside the plasma.

## 2. Experimental setup and data

MAST is a spherical tokamak with a major radius  $R_0 \approx 0.85$  m and a minor radius of  $a \approx 0.65$  m, magnetic field strength is about 0.5 T with the toroidal,  $B_t$ , and the poloidal,  $B_p$ , field components giving a pitch angle of about  $22^\circ$  at the edge region. We analyse data from an Ohmic plasma discharge numbered 29150, with a line average number density,  $n \approx 1.47 \times 10^{19} \text{ m}^{-3}$ , and plasma current  $I_p = 0.43$  MA. No additional heating power was applied during the discharge. Magnetic configuration was that of a double null.

The data was collected using a Mach type reciprocating Langmuir probe [26], on the outboard mid-plane, measuring floating potential,  $\tilde{V}_f$  as well a set of ion saturation currents (pins 2, 5 and 8). Figure 1 shows the schematic of the probe, with pin numbers and the relative distances between them.

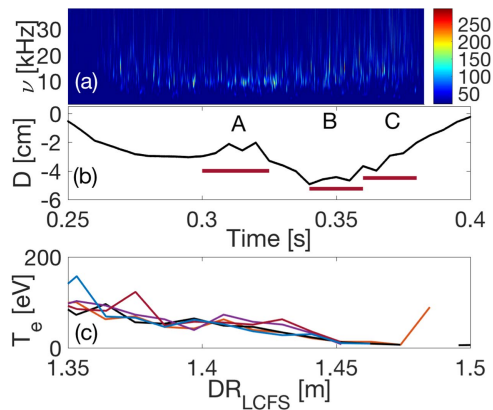
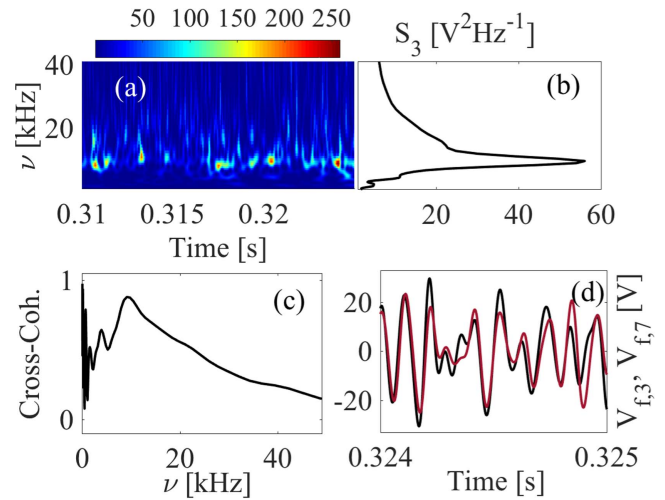


**Figure 2.** Summary of the data. (a) Wavelet power at lower frequencies. (b) Mach probe distance from the last closed flux surface (LCFS); negative values indicate position inside the plasma. Horizontal red lines mark three time intervals analysed here. (c) Electron temperature profiles from Thomson scattering system between 0.32 and 0.36 s.

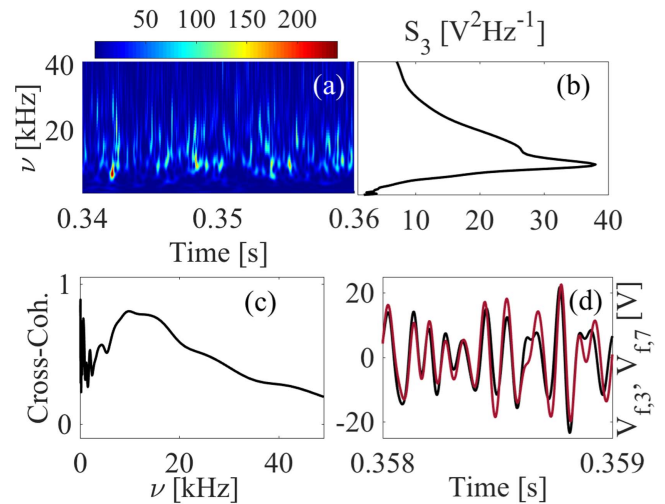
Pins (1, 3) are positioned 8 mm behind pin pairs (4, 6) and (7, 9). The floating potential  $\tilde{V}_f$  is taken as a proxy of the plasma potential  $\tilde{V}_p$ . These are related by  $\tilde{V}_p = \tilde{V}_f + \Lambda$ , where  $\Lambda$  is the sheath potential drop, which is a slowly varying function of the electron and ion temperatures and is usually approximated by  $\Lambda \approx 2.5 T_e/e$  (see, for example [27] and references therein). The Mach barrier can modify plasma flows as well as the electron and the ion temperatures, due to the sheath potential. The measurement of  $\tilde{V}_f$  is based on the plasma balancing ion and electron currents, which in principle should not depend on the flow, but only on the plasma temperature. In addition, it is assumed that the electrostatic potential fluctuations are larger than these due to electron/ion temperature fluctuations. These assumptions are supported by the high values of temporal correlations on all pin pairs, with correlation coefficients between 0.65 and 0.95. This includes pin pairs separated by the Mach barrier, for example pair (4, 7). We have chosen pin pairs (3, 7) and (7, 9) for our analysis, due to their high cross-correlation coefficient and their approximate alignment on one side of the Mach barrier.

Figure 2 presents a summary of the data. Panel (a) shows wavelet power in the floating potential of pin 3 as a function of time. We observe a clear but intermittent increase in power for a relatively narrow frequency range of  $\sim 9$  to  $\sim 15$  kHz between times 0.30 and 0.39 s of the discharge. We have verified that there is no significant magnetic activity at this time. Panel (b) of figure 2 shows the distance of the Mach probe in relation to the last closed flux surface (LCFS). The probe is inside the plasma and reaches the maximum radial depth of about 4.5 cm at the time of 0.35 s. Panel (c) of figure 2 shows electron temperature from Thomson scattering diagnostic at the time of interest. It gives the electron temperature at the probe location of the interval A in the range of  $T_e \approx 8$  eV to  $T_e \approx 60$  eV, with the median at  $T_e \approx 14$  eV. We take the electron temperature at  $T_e = 10$  eV. The proton gyroradius at this electron temperature is  $\rho_p = 0.15$  cm.

We analyse floating potential data,  $\tilde{V}(\mathbf{r}_i, t)$ , where  $i = 3, 7, 9$  indicates the relevant pin number and vector  $\mathbf{r}$  is a



**Figure 3.** Summary of the data for interval A. (a) Wavelet power at lower frequencies, units ( $V^2 \text{Hz}^{-1}$ ). (b) Integrated wavelet power. (c) Linear cross coherence of the floating potential from pins 3 and 7. (d) Time series of the floating potential from pins 3 (black line) and 7 (red line) for small time subinterval.



**Figure 4.** Same as figure 3, but for interval B.

position of each pin. We choose three intervals spanning periods 0.30–0.325, 0.34–0.36 and 0.36–0.38 s when the probe distance to the LCSF is relatively stable. We will refer to these intervals as A, B and C. The average probe position in each interval is  $D_A = -2.53$  cm,  $D_B = -4.00$  cm and  $D_C = -3.14$  cm. Each interval contains at least  $1 \times 10^4$  samples. Numerical simulations of L-mode discharge with realistic shaping parameters found strong GAM oscillations in a broad range of radii ( $0.9 < \psi^{1/2} < 1$ ), with the maximum of power located at  $0.95 < \psi^{1/2} < 0.975$ , for the 10 kHz harmonic [19]. In addition, previous analysis of MAST reciprocating probe data identified a strong 10 kHz signal with a GAM-like dispersion relation [17]. Based on these findings, we interpret observed 9–11 kHz oscillations as the GAM.

Figures 3 and 4 show details of spectral and temporal features of the data for intervals A and B, respectively. Both figures show: wavelet power in panels (a), time integrated

wavelet power spectrum in panels (b) (for the same frequencies given on the  $y$ -axis in panels (a)), linear cross coherence in panels (c) and a short time series of the floating potential  $\tilde{V}(\mathbf{x}_3, t)$  and  $\tilde{V}(\mathbf{x}_7, t)$  filtered between 5 and 15 kHz, in panels (d). We note a significant difference in the power spectra of the intervals  $A$  and  $B$ . Interval  $A$  has a narrow spectral peak at  $\sim 10$  kHz, while the spectral peak of interval  $B$  is much broader, with significant power in the range of  $\sim 9$ –15 kHz. Various numerical simulations demonstrated the emergence of frequency plateaus spanning some fraction of a minor radius, with higher harmonic plateaus sometimes overlapping in their location with the fundamental one [19]. The power distribution of interval  $B$  is consistent with a double plateau at  $\sim 10$  and  $\sim 15$  kHz. Panels (d) of figures 3 and 4 demonstrate that the signals on both pins are similar, and that the phase shift between these varies, but is always smaller than the wavelength of the large amplitude fluctuations.

### 3. The Methodology

We apply the data analysis technique, which uses a two-point instantaneous phase difference to extract the wave number from the signal. Ordinarily, this technique is used when the connection vector  $\mathbf{d} = \mathbf{r}_1 - \mathbf{r}_2$  between the measurements points  $\mathbf{r}_1$  and  $\mathbf{r}_2$  is approximately aligned with the wave vector. In such case, an estimate of the wave vector projection on the connection vector  $k_p = \mathbf{k}(\nu) \cdot \mathbf{d}$  is obtained in four steps. First, the wavelet transform is calculated giving a coefficient  $W(\mathbf{r}_i, \nu, \tau)$  for each frequency  $\nu$  (scale) at each measurement time  $\tau$ . Second, the instantaneous cross-spectral density,  $H(\mathbf{d}, \nu, \tau)$  is obtained as follows:

$$H(\mathbf{d}, \nu, \tau) = W^*(\mathbf{r}_1, \nu, \tau)W(\mathbf{r}_2, \nu, \tau) = |W| \exp(i\phi). \quad (1)$$

The last equality expresses the complex quantity  $H(\mathbf{d}, \nu, \tau)$  in polar representation and defines the instantaneous phase as  $\phi(\mathbf{d}, \nu, \tau) = \arctan[\Im(H(\mathbf{d}, \nu, \tau)) / \Re(H(\mathbf{d}, \nu, \tau))]$ . The third step gives an estimate of the projected wave number

$$k_p(\nu) \approx \frac{\phi(\nu)}{d}. \quad (2)$$

Finally, having established a relation between the wave number and the frequency, a histogram of power at each  $(k_p, \nu)$  pair is constructed according to

$$S(k_p, \nu) = \left\langle \frac{1}{2} (|W(\mathbf{r}_1, \nu, \tau)|^2 + |W(\mathbf{r}_2, \nu, \tau)|^2) \delta(k - k_p) \right\rangle, \quad (3)$$

where angular brackets now indicate an ensemble average over all measurement points. Note that, since all results will use frequency  $\nu$  (in kHz), rather than the angular frequency  $\omega$ , we have deviated from the standard notation and used frequency in the above equations. In practice,  $S(k_p, \nu)$  is calculated by binning instantaneous power given by (6) into a discretised  $(k_p, \nu)$  plane. The wavenumber–frequency spectrum  $S(k_p, \nu)$ , when examined visually, can reveal multiple dispersion relations in the system. The definition of

the projected wave number (2) introduces a natural ambiguity of  $2j\pi$  ( $j \in \mathbb{Z}$ ) and, in principle, the domain of  $k_p$  spans an infinite number of negative and positive values of  $j$ . The visual inspection of the  $S(k_p, \nu)$  plot can easily reveal if such an ambiguity is present.

The basic method described above cannot yield the radial wave number in the case of Mach probe data, without further assumptions. Indeed, the radial separation of pins 3 and 7 is comparable to their poloidal separation and the wave vector direction is not, in principle, aligned with the overall separation vector. For such a configuration and with a radial wave number component pointing towards the LCFS, any finite wave vector component  $\pm k_\theta$  reduces or increases the value of the projected wave number  $k_p$ , depending on the sign of the poloidal wave number. Indeed, for an extreme case of  $k_r = k_\theta$  the projection on the separation vector of pins (3, 7) can be nearly zero. In principle, the poloidal wave number can be neglected, for fluctuations near the GAM frequency range [24], since the dominant poloidal mode has  $m = \pm 1$ , or  $k_\theta \sim a^{-1}$ , where  $a$  is the minor radius of the device. In our case this gives  $k_\theta \rho_p \sim \pm 0.0023$ . However, the presence of turbulent fluctuations with non-zero  $k_\theta$  numbers can contribute to the average  $k_p$  for small pin separation and we will show below that in our case the distribution  $S(k_p, \nu)$  gives a poor approximation of the radial wave number.

In order to account for the possible influence of  $k_\theta$  on the estimate of the radial wave number, we use the full distribution of power in  $S(k_r, k_\theta, \nu)$ , and construct a reduced distribution  $S(k_r, \nu)$ , by averaging the joint spectrum over the distribution of  $S(k_\theta, \nu)$ . We now describe the details of the modified method, which uses pin pair (7, 9) to compensate for the poloidal wave number contribution to the radial wave number obtained from pair (3, 7). We have verified that pin pairs (1, 3) and (1, 9) give similar results.

As with the basic method, the instantaneous phase difference  $\phi(\nu, t)$  between spectral components of a signal is estimated from cross-coherence, constructed from the wavelet decomposition. The analysed data is a floating potential offset by its time average,  $V(\mathbf{r}_i, t) = \tilde{V}(\mathbf{r}_i, t) - \langle \tilde{V}(\mathbf{r}_i, t) \rangle_t$ . We assume that  $V(\mathbf{r}_i, t)$  is a zero-mean, stationary, homogeneous scalar field, which can be represented as a superposition of plane wave packets using wavelet decomposition with the wavelet coefficients given by

$$W(\mathbf{r}_i, s, \tau) = \int_{-\infty}^{\infty} dt V(\mathbf{r}_i, t) \frac{1}{\sqrt{s}} \psi^* \left( \frac{t - \tau}{s} \right), \quad (4)$$

where  $s$  is a scale,  $\tau$  is a new time label and  $\psi(t)$  are the analysing wavelets. We use Morlet wavelets defined as

$$\psi(t) = \frac{1}{\pi^{1/4}} \exp(-2\pi i t) \exp(-t^2/2), \quad (5)$$

which have good simultaneous time–frequency resolution and are mathematically identical to a Fourier transform with a short-time Gaussian window function. The scale  $s$  can be related to an instantaneous angular frequency  $\omega = 2\pi/s$ . The time averaged power spectrum of a single point data collected

at pin location  $\mathbf{r}_i$  is then expressed as

$$P(\mathbf{r}_i, \nu) = \langle W^*(\mathbf{r}_i, \nu, \tau) W(\mathbf{r}_i, \nu, \tau) \rangle_\tau. \quad (6)$$

Consider measurements of  $V(\mathbf{r}_3, t)$  and  $V(\mathbf{r}_7, t)$  and their instantaneous cross-spectral density,

$$H_{(3,7)}(\mathbf{d}, \nu, \tau) = W^*(\mathbf{r}_3, \nu, \tau) W(\mathbf{r}_7, \nu, \tau) = |W| \exp(i\phi_{(3,7)}). \quad (7)$$

The instantaneous phase  $\phi(\mathbf{d}, \nu, \tau) = \arctan[\Im(H_{(3,7)}(\mathbf{d}, \nu, \tau)) / \Re(H_{(3,7)}(\mathbf{d}, \nu, \tau))]$  must account for the full separation vector of these pins, that is

$$\phi_{(3,7)}(\mathbf{d}, \nu, \tau) = \mathbf{k}(\nu) \cdot \mathbf{d} = k_r d^r + k_\theta d^\theta + k_\zeta d^\zeta, \quad (8)$$

where subscripts ( $r, \theta, \zeta$ ) correspond to radial, poloidal and toroidal directions, respectively.

In what follows we assume the toroidal symmetry of the low frequency modes and neglect the term  $k_\zeta d^\zeta$  in (8). We account for the poloidal wave number contribution to  $\phi_{(3,7)}$  by considering pin pair with poloidal and toroidal (neglected) separations only, here pair (7, 9). Neglecting toroidal mode number we obtain poloidal wave number

$$k_\theta = \frac{\phi_{(7,9)}}{d_{(7,9)}^\theta}. \quad (9)$$

Substituting this to (8) we obtain the corrected estimation of the radial wave number  $k_r$ , for a given value of  $k_\theta$ :

$$k_r = \frac{\phi_{(3,7)}}{d^r} - \left( \frac{\phi_{(7,9)} d_{(3,7)}^\theta}{d_{(7,9)}^\theta d_r} \right). \quad (10)$$

The relations  $k_r(\nu, \tau)$  and  $k_\theta(\nu, \tau)$  allow us to construct the joint wavenumber–frequency spectrum  $S_{(3,7)}(k_r, k_\theta, \nu)$ :

$$S_{(3,7)}(k_r, k_\theta, \nu) = \langle (|W(\mathbf{r}_3, \nu, \tau)|^2 + |W(\mathbf{r}_7, \nu, \tau)|^2) \delta(k - k_r) \delta(k - k_\theta) \rangle_\tau. \quad (11)$$

The equivalent quantity computed from the pair (7, 9) is simply given by

$$S_{(7,9)}(k_\theta, \nu) = \langle (|W(\mathbf{r}_7, \nu, \tau)|^2 + |W(\mathbf{r}_9, \nu, \tau)|^2) \delta(k - k_\theta) \rangle_\tau. \quad (12)$$

Using the usual definition of a reduced probability distribution, we then obtain an approximate spectrum of radial wave numbers at a given frequency,

$$S_{(3,7)}(k_r, \nu) = \sum_{k_\theta} S_{(3,7)}(k_r, k_\theta, \nu). \quad (13)$$

We assume that the Doppler shift at these low frequencies is small and can be neglected. When the wave vector is approximately aligned with the separation vector of the pin pair, this direction can be verified by the visual inspection of the signals on both pins. In our case, this is not possible since both radial and poloidal wave numbers contribute to the phase shift.

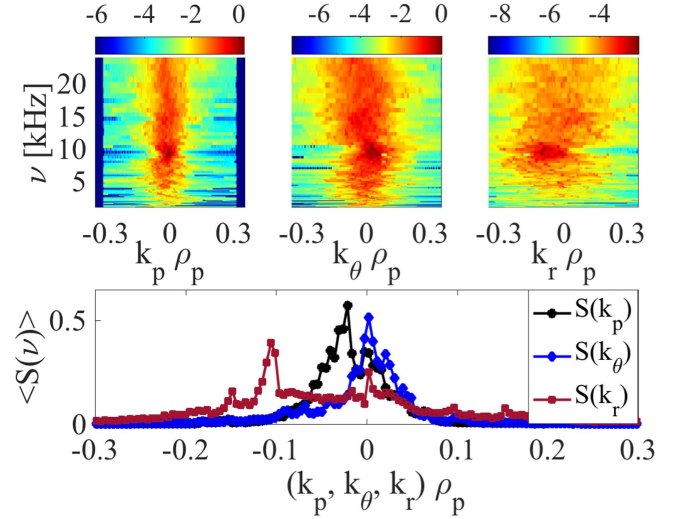


**Figure 5.** Top row: comparison of the wave number–frequency spectra for: (left) total wave number projected onto the separation vector as given by (3), (centre) averaged poloidal wave number from pin pairs (1, 3) and (7, 9) and (right) radial wave number calculated from (10), (11) and (13). Lower panel: power integrated over seven consecutive frequency cuts,  $9.2 \leq \nu \leq 11.2$  through each wave number–frequency spectra shown in the top row. Black circles:  $S(k_p)$ , blue diamond:  $S(k_\theta)$  and red squares:  $S(k_r)$ .

## 4. Results and discussion

Before we discuss results obtained for different intervals, we use interval A to demonstrate the difference between the wave number–frequency spectra constructed by different methods. In the following, we have dropped the subscripts indicating the pin pairs for the wavenumber–frequency spectra as these should be clear from the arguments given in the parenthesis. The top row of figure 5 shows three wave number–frequency spectra: on the left is the spectrum  $S(k_p, \nu)$  calculated by expression (3), that is, finding the projection of the total wave number on the separation vector. At the centre, we plot the poloidal wave number spectrum from pin pair (7, 9) and on the right we show  $S(k_r, \nu)$  calculated from (10), (11) and (13). These histograms of power have been constructed by dividing the frequency domain into 189 dyadic bins, and dividing the allowed wave number domain of  $(-\pi/d, \pi/d)$  into 256 uniform bins. This gives the wave number resolution of  $\Delta k \approx 0.03 \text{ cm}^{-1}$ , which corresponds to about twice the wave number of  $m = \pm 1$  mode at the geodesic of the edge of MAST plasma,  $k_\theta \rho_p \sim 0.0023$ . We note that the colour scale corresponds to  $\log_{10}(S)$ , and it has been forced to display power near its maximum level, for clarity. The narrow wavenumber range of  $S(k_p)$  is due to projection effect.

The lower panel of figure 5 shows an average power  $\langle S(k_p) \rangle_\nu$ ,  $\langle S(k_\theta) \rangle_\nu$ , and  $\langle S(k_r) \rangle_\nu$ , calculated for the range of frequencies near the GAM spectral peak, 9.5–11.5 kHz. We first note that the maximum of  $\langle S(k_\theta) \rangle_\nu$ , is located near zero, as expected for  $m = \pm 1$  GAM mode. We observe a clear peak in the  $\langle S(k_r) \rangle_\nu$  curve at about  $k_r \rho_p \sim 0.11$ , while the average of the projected wave number spectrum peaks at a much lower value of  $k_p \rho_p \sim 0.025$ .

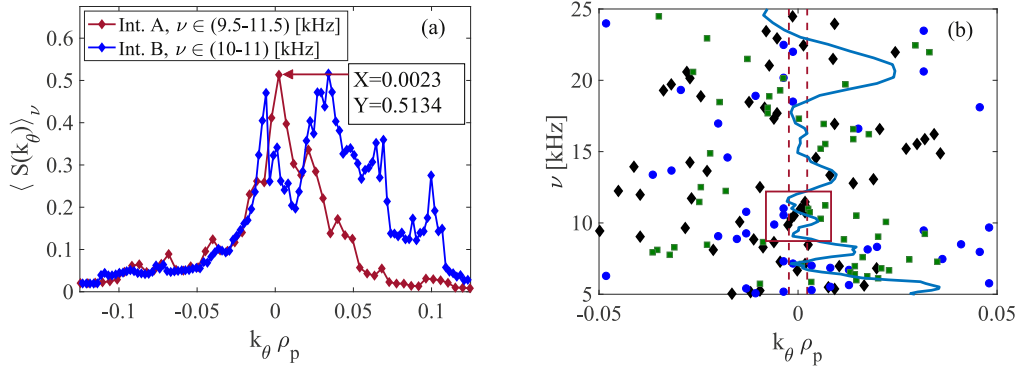


**Figure 6.** (a) Averaged power in  $S(k_\theta, \nu)$  for interval A at frequencies  $9.5 \leq \nu \leq 11.5$  kHz (red) and for interval B at frequencies  $10 \leq \nu \leq 11$  kHz (blue). (b) Locations of maxima in power in the  $(k_\theta, \nu)$  plane for interval A (black diamonds), interval B (blue circles) and interval C (green squares). Vertical dashed lines mark the approximate frequency of  $m = \pm 1$  mode and the red box shows the range of frequencies used in obtaining the average power level at a radial wave number  $k_r$  in the figure 7(c). Light blue solid line shows averaged poloidal wave number  $k_\theta$  for interval A.

The identification of the  $m = \pm 1$  mode is essential to finding an appropriate range of frequencies where GAM is dominant, or at least significant. In order to quantify the contribution of the  $m = \pm 1$  mode in each interval we examine the  $S(k_\theta, \nu)$  spectrum calculated at the higher resolution of 350 frequency bins and 512 wave number bins. Panel (a) of figure 6 shows the average power  $\langle S(k_\theta) \rangle_\nu$  for intervals A and B near the GAM frequency. In the case of interval A (red curve), the maximum power is unambiguously located at the bin containing  $m = \pm 1$  mode, that is  $k_\theta \rho_p \sim 0.0023$ , but a second significant peak is also visible at  $k_\theta \rho_p \sim 0.02$ . The equivalent curve for the interval B is broader, with the maximum power at  $k_\theta \rho_p \sim 0.03$ , but a significant power is clearly detectable at bins containing  $k_\theta \rho_p \sim -0.006$  and  $k_\theta \rho_p \sim 0.0023$ . In panel (b) we show a scatter plot of the maxima in  $S(k_\theta, \nu)$  spectrum. The vertical dashed lines mark the interval  $|k_\theta \rho_p| \leq 0.0023$  and a red square in this graph gives a range of frequencies, for which  $k_\theta \rho_p$  approaches  $\pm 0.0023$ . Interval A exhibits the clearest clustering of power at  $|k_\theta \rho_p| \leq 0.0023$  and around GAM frequencies of 9.2–10.5 kHz, with intervals B and C showing similar, but not as clear, behaviour. We note that on the scale of the Mach probe pin separation, around 1 cm, the average poloidal wave number measured by pins (7, 9) does not show any decrease towards 0 at frequencies around 10 kHz. In order to check if the small pin separation is indeed a contributing factor to the averaged poloidal wave number measurements, we have constructed the poloidal wave number-frequency spectrum from pins (1, 9), using the expression  $k_\theta^{(1,9)} = (\phi_{(3,7)} - \phi_{(1,9)}) / (d_{(3,7)}^\theta - d_{(1,9)}^\theta)$ . Pins (1,9) have poloidal separation of  $\sim 2.5$  cm. The average (over 4 consecutive frequency bins) wave number  $\langle k_\theta^{(1,9)} \rangle$  is shown as the solid light blue line in figure 6(b). Clearly, on these larger scales the dominant wave number at the GAM frequency is that of  $m = \pm 1$  mode.

Figure 7 presents the main result of our study in the format similar to that of figure 5. The top row shows reduced wave number-frequency spectra  $S(k_r, \nu)$  for all three intervals, ordered from A on the left to C on the right. While the distribution of power for the interval A is narrow and peaks

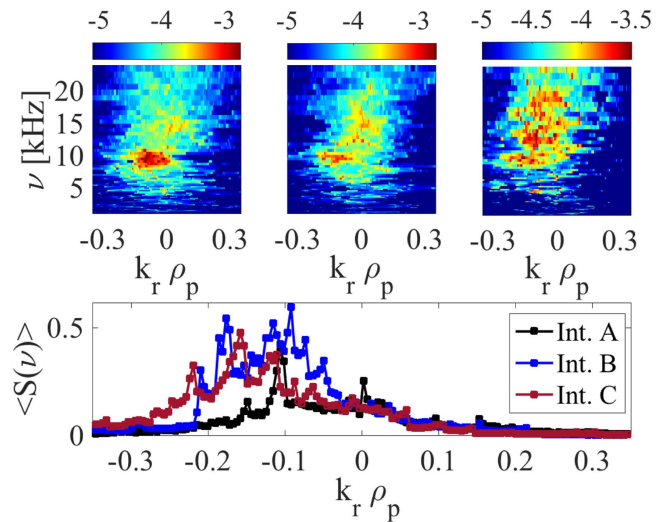


**Figure 7.** Top row: the wave number-frequency spectra  $S_{(3,7)}(k_r, \nu)$  for: (left) interval A, (centre) interval B and (right) interval C. Lower panel: power integrated over seven consecutive frequency cuts through each wave number-frequency spectra shown in the top row. Blue diamond: interval A, black circles: interval B and red squares: interval C.

strongly around GAM frequencies, the  $S(k_r, \nu)$  spectra for intervals B and C are broader and show high levels of power near  $\sim 10$  and  $\sim 15$  kHz, suggesting that a 10 kHz signal represents a second harmonic of a low power  $\sim 5$  kHz mode. We note that the linear theory predicts zero amplitude of the fundamental GAM harmonic at the mid-plane, but a non-linearly generated second harmonic would have maximum amplitude at this location [28].

The bottom panel shows average power in  $\langle S(k_r) \rangle_\nu$  for the range of frequencies spanning the rectangular box in figure 6(b). This spectrum broadens significantly when the probe moves deeper into the plasma. The maxima of these spectra give an estimate of the most likely value of the radial wave number for the GAM. We find a single peak at about  $-0.11$  for the interval A, and a broader distribution for the

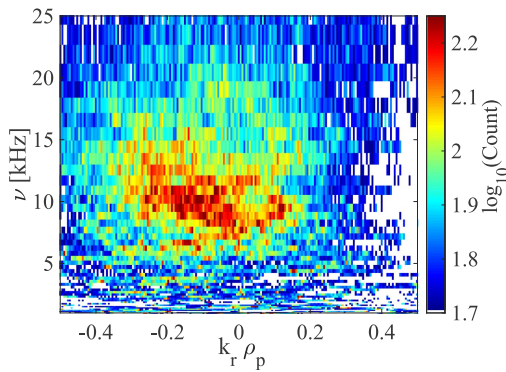


**Figure 8.** Number of samples contributing to  $S(k_r, \nu)$  of interval A.

intervals B and C, spanning values between  $k_r \rho_p \approx -(0.1-0.2)$ . We note that we are not able to establish a clear direction of propagation from two-point measurement using the current configuration.

It is rather difficult to construct an error estimate for the  $S(k_r, \nu)$  spectrum. As a statistically averaged quantity,  $S(k_r, \nu)$  can show high values from singular large amplitude fluctuations, which can be rare and thus not statistically significant. In order to make sure that the estimated power comes from the statistically significant number of fluctuations we construct a count histogram, which quantifies a number of samples contributing to each  $(k_r, \nu)$  pair of interval A. This histogram is shown in the figure 8. The colour map corresponds to the logarithm of counts. It is clear that there are large number of samples detected in the region of maximal power in  $S(k_r, \nu)$ . We conclude that the maximal radial wave number of GAM-like fluctuations at frequency  $\nu \approx 10$  kHz is  $k_r = -1.15$  ( $\text{cm}^{-1}$ ). This corresponds to wavelength of  $\lambda \approx 6$  cm. The estimated phase velocity is in the range of  $v^{\text{ph}} \approx 1$  km  $\text{s}^{-1}$ . These values are lower than, but broadly consistent with results obtained from the multi-fluid simulations for MAST L-mode discharges [19], and with the values measured in other mid-size tokamaks [24, 25]. Measured  $k_r$  values allow estimation of the shearing rate of the oscillatory flows, which is approximately given as  $\gamma_{\text{sh}} \approx k_r v_{\theta, \text{GAM}}$ . We calculate  $v_{\theta, \text{GAM}} \approx (\Delta E_r)/B_0$ , where  $\Delta E_r$  is taken as a standard deviation of the radial electric field  $E_r(t) \approx 0.5 * [V(\mathbf{r}_3, t) - V(\mathbf{r}_7, t)]/d'$  (the radial and poloidal separation for pins 3 and 7 are nearly the same). This gives an estimate  $v_{\theta, \text{GAM}} \approx 2 \times 10^3$  m  $\text{s}^{-1}$ , leading to  $\gamma_{\text{sh}} \approx 1 \times 10^4$  ( $\text{s}^{-1}$ ). This value is much smaller than a typical growth rate of the drift instability,  $\gamma_{\text{dr}} \approx 10^5$  ( $\text{s}^{-1}$ ).

## 5. Conclusions

In summary, we have obtained a first estimate of the radial wave number  $k_r$  of the GAM-like oscillatory flows in the Ohmic MAST edge plasma discharge. The GAM signal appears when the probe depth is about 2 cm into the plasma and the frequency is close to 10 kHz, in agreement with previous observations and numerical simulations [17, 19]. We find maximum radial mode number of  $k_r \rho_p \approx -0.15$ . This estimate gives the radial phase velocity of the GAM of

1 km  $\text{s}^{-1}$  and a shearing rate that is about one order of magnitude smaller than the typical growth rate of drift instability in MAST edge plasma.

## Acknowledgments

This work has been carried out within the framework of the EUROfusion Consortium and has received funding from the Euratom research and training programme 2014–2018 under grant agreement No. 633053 and from the RCUK Energy Programme [grant number EP/P012450/1]. The views and opinions expressed herein do not necessarily reflect those of the European Commission.

## ORCID iDs

B Hnat  <https://orcid.org/0000-0001-6498-2953>

F Militello  <https://orcid.org/0000-0002-8034-4756>

N Walkden  <https://orcid.org/0000-0002-0661-5909>

## References

- [1] Diamond P H, Itoh S I, Itoh K and Hahn T S 2005 *Plasma Phys. Control. Fusion* **47** R35
- [2] Rosenbluth M N and Hinton F L 1998 Poloidal flow driven by ion-temperature-gradient turbulence in tokamaks *Phys. Rev. Lett.* **80** 724
- [3] Lin Z, Hahn T S, Lee W W, Tang W M and White R B 1998 Turbulent transport reduction by zonal flows: massively parallel simulations *Science* **281** 1835–7
- [4] Terry P W, Newman D E and Ware A S 2001 Suppression of transport cross phase by strongly sheared flow *Phys. Rev. Lett.* **87** 185001
- [5] Rogers B N, Dorland W and Kotschenreuther M 2000 Generation and stability of zonal flows in ion-temperature-gradient mode turbulence *Phys. Rev. Lett.* **85** 5336
- [6] Moyer R A, Tynan G R, Holland C and Burin M J 2001 Increased nonlinear coupling between turbulence and low-frequency fluctuations at the L-H Transition *Phys. Rev. Lett.* **87** 135001
- [7] Tynan G R, Moyer R A, Burin M J and Holland C 2001 On the nonlinear turbulent dynamics of shear-flow decorrelation and zonal flow generation *Phys. Plasmas* **8** 2691–9
- [8] Hasegawa A and Wakatani M 1987 Self-organization of electrostatic turbulence in a cylindrical plasma *Phys. Rev. Lett.* **59** 1581
- [9] Winsor N, Johnson J L and Dawson J M 1968 Geodesic acoustic waves in hydromagnetic systems *Phys. Fluids* **11** 2448–50
- [10] Lakhin V P, Ilgisonis V I and Smolyakov A I 2010 Geodesic acoustic modes and zonal flows in toroidally rotating tokamak plasmas *Phys. Lett. A* **374** 4872–5
- [11] Gao Z 2010 Plasma shaping effects on the geodesic acoustic mode in the large orbit drift width limit *Phys. Plasmas* **17** 092503
- [12] Ilgisonis V I, Khalzov I V, Lakhin V P, Smolyakov A I and Sorokina E A 2014 Global geodesic acoustic mode in a tokamak with positive magnetic shear and a monotonic temperature profile *Plasma Phys. Control. Fusion* **56** 035001

- [13] Jakubowski M, Fonck R J and McKee G R 2002 Observation of coherent sheared turbulence flows in the DIII-D tokamak *Phys. Rev. Lett.* **89** 265003
- [14] Silva C, Arnoux G, Groth M, Hidalgo C, Marsen S and JET-EFDA Contributors 2012 Observation of geodesic acoustic modes in the JET edge plasma *Plasma Phys. Control. Fusion* **55** 025001
- [15] Ido T *et al* 2006 *Plasma Phys. Control. Fusion* **48** S41
- [16] Conway G D, Trřster C, Scott B and Hallatschek K 2008 Frequency scaling and localization of geodesic acoustic modes in ASDEX Upgrade *Plasma Phys. Control. Fusion* **50** 055009
- [17] Robinson J R, Hnat B, Dura P, Kirk A, Tamain P and MAST Team 2012 Interaction between a low-frequency electrostatic mode and resonant magnetic perturbations in MAST *Plasma Phys. Control. Fusion* **54** 105007
- [18] Miyato N, Kishimoto Y and Li J Q 2006 Nonlocal behaviour of zonal flows in tokamak plasmas *Plasma Phys. Control. Fusion* **48** A335
- [19] Robinson J R, Hnat B, Thyagaraja A, McClements K G, Knight P J, Kirk A and MAST Team 2013 Global two-fluid simulations of geodesic acoustic modes in strongly shaped tight aspect ratio tokamak plasmas *Phys. Plasmas* **20** 052302
- [20] Scott B 2003 The geodesic transfer effect on zonal flows in tokamak edge turbulence *Phys. Lett. A* **320** 53–62
- [21] Miki K and Diamond P H 2010 Role of the geodesic acoustic mode shearing feedback loop in transport bifurcations and turbulence spreading *Phys. Plasmas* **17** 032309
- [22] Itoh K, Itoh S I, Diamond P H, Fujisawa A, Yagi M, Watari T, Nagashima Y and Fukuyama A 2006 Geodesic acoustic eigenmodes *Plasma Fusion Res.* **1** 037
- [23] Beall J M, Kim Y C and Powers E J 1982 Estimation of wavenumber and frequency spectra using fixed probe pairs *J. Appl. Phys.* **53** 3933–40
- [24] Liu A D *et al* 2009 Characterizations of low-frequency zonal flow in the edge plasma of the HL-2A tokamak *Phys. Rev. Lett.* **103** 095002
- [25] Zhao K J *et al* 2006 Toroidal symmetry of the geodesic acoustic mode zonal flow in a tokamak plasma *Phys. Rev. Lett.* **96** 255004
- [26] MacLatchy C S, Boucher C, Poirier D A and Gunn J 1992 Gundestrup: a Langmuir/Mach probe array for measuring flows in the scrape-off layer of TdeV *Rev. Sci. Instrum.* **63** 3923–9
- [27] Tamain P, Kirk A, Nardon E, Dudson B and Hnat B 2010 Edge turbulence and flows in the presence of resonant magnetic perturbations on MAST *Plasma Phys. Control. Fusion* **52** 075017
- [28] Sasaki M, Itoh K, Nagashima Y, Ejiri A and Takase Y 2009 Nonlinear self-interaction of geodesic acoustic modes in toroidal plasmas *Phys. Plasmas* **16** 022306